Journal of Solid State Chemistry 181 (2008) 2155–2160

Contents lists available at ScienceDirect

Journal of Solid State Chemistry

journal homepage: www.elsevier.com/locate/jssc

# Synthesis and study of the crystallographic and magnetic structure of $DyFeMnO_5$: A new ferrimagnetic oxide

M.J. Martínez-Lope [a], M. Retuerto [a], J.A. Alonso [a,*], V. Pomjakushin [b]

[a] Instituto de Ciencia de Materiales de Madrid, CSIC, Cantoblanco, E-28049 Madrid, Spain
[b] Laboratory for Neutron Scattering, ETHZ & PSI, CH-5232 Villigen PSI, Switzerland

ARTICLE INFO

*Article history:*
Received 2 April 2008
Received in revised form
6 May 2008
Accepted 7 May 2008
Available online 15 May 2008

*Keywords:*
$RMn_2O_5$
Multiferroic oxides
Magnetoelectric
Ferrimagnetic
Neutron diffraction
Magnetic structure

ABSTRACT

The title oxide has been obtained by replacing $Mn^{3+}$ by $Fe^{3+}$ in the parent oxide $DyMn_2O_5$. The crystallographic and magnetic structures have been analysed from neutron powder diffraction (NPD) data, in complement with susceptibility and magnetic measurements. $DyFeMnO_5$ is orthorhombic, belonging to the *Pbam* space group as the parent compound. The crystal structure contains infinite chains of edge-sharing $Mn^{4+}O_6$ octahedra, interconnected by dimer units of $Fe^{3+}O_5$ square pyramids. There is a certain antisite disorder in the crystal structure, with 8.0% of the $Mn^{4+}$ sites occupied by Fe cations, and 8.2% of the $Fe^{3+}$ positions occupied by $Mn^{3+}$ cations. The magnetization measurements show that $DyFeMnO_5$ presents magnetic order below $T_C \approx 178$ K; a study of the magnetic structure from the low-temperature NPD patterns indicates an antiferromagnetic coupling of the $Mn^{4+}$ and $Fe^{3+}$ spins, with the polarization of the $Dy^{3+}$ magnetic moments parallel to the those of the Fe sublattice.



## 1. Introduction

The magnetoelectric (ME) oxides have been studied for many decades because of the technologically important possibility of controlling the dielectric properties using a magnetic field [1–3]. Unfortunately, compounds showing large ME effects are extremely rare. Recent discoveries of giant ME effects in hexagonal $RMnO_3$ and $RMn_2O_5$ ($R$ is Tb, Ho, or Dy) have led to a dramatic renaissance in the field [4–7]. The physical origin of this phase complexity lies in the partially competing interactions between the $Mn^{4+}/Mn^{3+}$ spins, the rare earth magnetic moments and the lattice degrees of freedom [8]. Very recently, a striking correlation between ferroelectric and magnetic order has been found in $TbMn_2O_5$ [4,6].

The orthorhombic crystal structure of the $RMn_2O_5$ compounds (space group *Pbam*) is attractive because it contains two crystallographic sites for Mn atoms, with different oxygen coordinations and oxidation states [9–11]. $Mn^{4+}$ are located at the 4*f* sites, octahedrally coordinated to oxygens, whereas $Mn^{3+}$ ions occupy the 4*h* sites and they are bonded by five oxygens, forming a distorted tetragonal pyramid. The crystallographic structure can be described as infinite chains of edge-sharing $Mn^{4+}O_6$ octahedra arranged along the *c*-axis; the chains are linked by pairs of $Mn^{3+}O_5$ corner-sharing pyramids. The neutron diffraction data indicated the onset of an antiferromagnetic order [12,13] with a $T_N = 40$ K. These oxides exhibit a complex magnetic structure defined by $k = (\frac{1}{2}, 0, k_z)$, where the incommensurate component $k_z$, depends on the rare earth $R$ size and also on the temperature, in such a way that in certain cases, $k_z$ can attain a commensurate value. Recently, aiming to induce new magnetic interactions in the $RMn_2O_5$ oxides, we have prepared some members of a new series of compounds of stoichiometry $RFeMnO_5$ ($R$ = Y, Ho, Er) [14–16], which are obtained by replacing $Mn^{3+}$ by $Fe^{3+}$ in $RMn_2O_5$. These oxides are ferrimagnetic below $T_C \approx 160$–$170$ K.

In this paper we describe a new member of this family, $DyFeMnO_5$. This oxide must be prepared under high $O_2$ pressure in order to stabilize $Mn^{4+}$, and it has been characterized from the structural and magnetic point of view from NPD data, complemented with macroscopic magnetic susceptibility measurements.

## 2. Experimental

Stoichiometric amounts of analytical grade $Dy_2O_3$, $FeC_2O_4 \cdot 2H_2O$ and $MnCO_3$ were dissolved in citric acid; the solution was slowly evaporated, and the obtained organic resin was dried at 120 °C and slowly decomposed at temperatures up to 600 °C in air, giving rise to very reactive and homogeneous precursor powders. Subsequent high oxygen pressure treatments were performed in a VAS furnace. About 2 g of the precursor powder were contained in

* Corresponding author. Fax: +34 91 372 06 23.
*E-mail address:* ja.alonso@icmm.csic.es (J.A. Alonso).

0022-4596/$ - see front matter © 2008 Elsevier Inc. All rights reserved.
doi:10.1016/j.jssc.2008.05.009

a gold can during the oxygenation process. The sample was slowly heated up to 900 °C at a final pressure of 200 bar, and held at this temperature for 12 h. The product was finally cooled, under pressure, at 300 °C $h^{-1}$ down to room temperature. Finally, the oxygen pressure was slowly released.

The initial characterization of the product was carried out by laboratory X-ray diffraction (XRD) (Cu$K\alpha$, $\lambda = 1.5406$ Å). Neutron powder diffraction (NPD) diagrams were collected at the HRPT diffractometer of the SINQ spallation source, at ETH-Zurich. The patterns were collected at room temperature with a wavelength of 1.494 Å, in order to study the crystal structure, and at 10 K with a wavelength of 1.886 Å, in order to investigate the magnetic structure. The high-flux mode was used; the collection time was 9 h. A double-walled vanadium sample holder was employed to minimize absorption. The refinement of the crystal and magnetic structures was performed by the Rietveld method [17], using the FULLPROF refinement program [18]. A pseudo-Voigt function was chosen to generate the line shape of the diffraction peaks. The following parameters were refined in the final runs: scale factor, background coefficients, zero-point error, pseudo-Voigt corrected for asymmetry parameters, positional coordinates and isotropic thermal factors. The absorption of the $DyFeMnO_5$ sample was measured, yielding a $\mu R$ value of 0.037, which was considered during the refinement. The coherent scattering lengths for Dy, Fe, Mn and O were 16.9, 9.45, −3.73 and 5.803 fm, respectively.

The magnetic measurements were performed in a commercial SQUID magnetometer from Quantum Design. The dc magnetic susceptibility was measured in both zero-field cooling (ZFC) and field cooling (FC) conditions in the temperature intervals 1.8 K < $T$ < 350 K, respectively, under a magnetic field of 1 kOe. ac magnetic susceptibility measurements were carried out in a PPMS device for temperatures 1.8 K < $T$ < 250 K; the frequencies for the transversal oscillating magnetic field were 0.32, 7, 33, 321 and 997 Hz. Isothermal magnetization curves were recorded at $T = 2$, 100, 175 and 250 K for magnetic fields ranging from −50 to 50 kOe.

## 3. Results

$DyFeMnO_5$ was obtained as a dark brown, polycrystalline powder. Fig. 1 shows the XRD pattern, which can be indexed in an orthorhombic unit-cell, isotypic to $RMn_2O_5$, with unit-cell parameters $a = 7.3136(7)$, $b = 8.5246(8)$, $c = 5.6927(5)$ Å. No additional peaks, which could indicate the presence of superstructures or departure of the mentioned symmetry, were observed. Minor impurities of the competitive $DyMnO_3$ phase were always identified in the pattern.

### 3.1. Magnetic properties

The dc susceptibility vs. temperature data, displayed in Fig. 2, indicate a long-range magnetic order below $T_C \approx 178$ K. The ZFC and FC curves, which overlap at high temperatures, split below 130 K. The ZFC susceptibility reaches a "plateau" at 3 K, as shown in the lower inset of Fig. 2. Below 20 K the FC curve undergoes a more pronounced increase. As it will be demonstrated by low-temperature NPD, the change in the slope at $T_C$ corresponds to the establishment of a ferrimagnetic structure. We believe that the extra increment of the FC susceptibility below 20 K is due to the long-range magnetic order of the $Dy^{3+}$ magnetic moments.

In the isothermal magnetization curves displayed in Fig. 3, a wide hysteresis loop (coercive field = 4000 Oe) is observed at $T = 2$ K with a remnant magnetization of 1.6$\mu_B$ per formula. A maximum magnetization of 7.11$\mu_B$/f.u. is reached for the

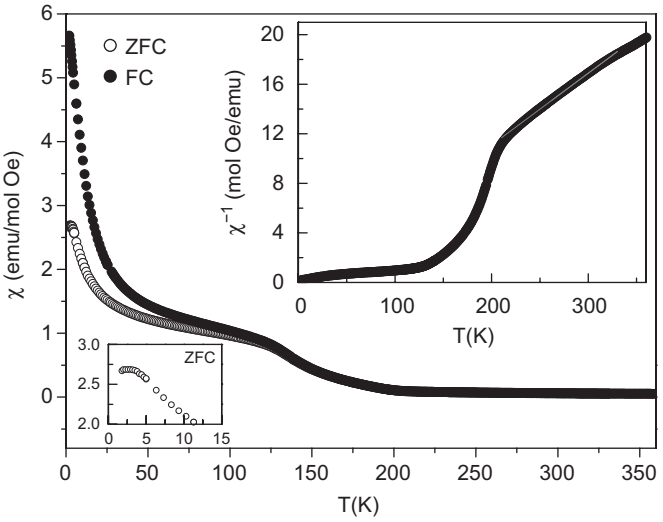


**Fig. 2.** Thermal evolution of the field cooling (FC) and zero field cooling (ZFC) dc susceptibility. Lower inset: close-up of the ZFC curve in the low $T$ region. Upper inset: reciprocal susceptibility (ZFC data).

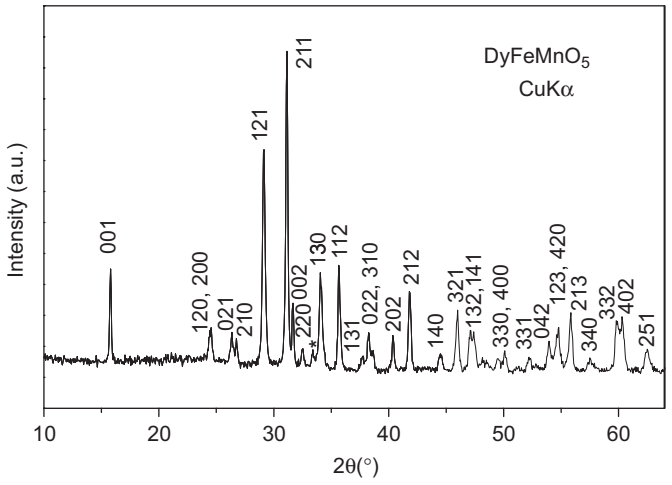


**Fig. 1.** XRD pattern of $DyFeMnO_5$, indexed in an orthorhombic unit cell with parameters $a = 7.3136(7)$, $b = 8.5246(8)$, $c = 5.6927(5)$ Å. The star indicates the main reflection of $DyMnO_3$ impurity.

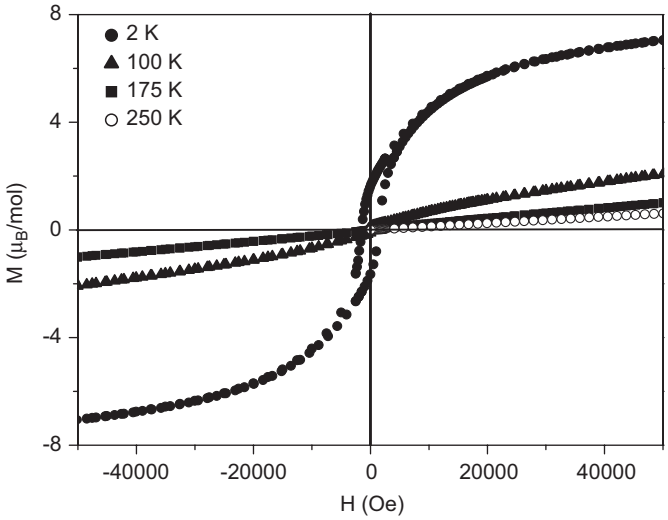


**Fig. 3.** Magnetization vs. magnetic field isotherms at $T = 2$, 100, 175 and 250 K.

maximum applied field of 50 kOe. The presence of a remnant magnetization is in good agreement with the thermal behaviour of the dc susceptibility below $T_C$ and with the ferrimagnetic order determined from NPD data, as described below. At 100 K the curve is still characteristic of a ferrimagnet with a remnant magnetization of $0.11\mu_B$ and a maximum magnetization of $2.07\mu_B$/f.u. at 5 T. At $T = 175$ and 250 K, the isothermal magnetization curves present a linear behaviour as it corresponds to a paramagnetic state.

The reciprocal magnetic FC susceptibility at temperatures above $T_C$ shows an abrupt change in the slope at 210 K, as displayed in the upper inset of Fig. 2. In the temperature interval $220 < T < 320$ K, the inverse of the susceptibility shows a linear behaviour that follows the Curie–Weiss law. An effective paramagnetic moment of $\mu_{eff} = 11.70(1)\mu_B$/f.u. and a paramagnetic temperature of $\theta_P = 9.29(8)$ K are determined from the Curie–Weiss fit. An estimation of the theoretical magnetic effective magnetic moment can be gained by considering the expression $\mu_{eff} = (\mu_B(Mn^{4+})^2+\mu_B(Fe^{3+})^2+\mu_B(Dy^{3+})^2)^{1/2}$; the effective magnetic moments for spin-only $Mn^{4+}$, high-spin $Fe^{3+}$ and $Dy^{3+}$ ($^6H_{15/2}$ ground state configuration) are 3.87, 5.92 and $10.63\mu_B$, respectively, which implies an effective magnetic moment of $12.77\mu_B$, in reasonable agreement with the experimental value.

The thermal evolution of the ac susceptibility is shown in Fig. 4 for temperatures ranging from 50 to 250 K at different frequencies. $\chi'$ and $\chi''$ represent, respectively, the real (in-phase) and imaginary (out of phase) components of the susceptibility. Both $\chi'$ and $\chi''$ present a maximum at around the long-range ordering temperature $T_C \approx 178$ K; however, another sharp peak is observed at lower temperatures, at around 130 K. This second anomaly is frequency dependent in both $\chi'$ and $\chi''$ curves. On increasing the frequency the intensity of the maximum decreases and the maximum position shifts to higher temperature. This behaviour is characteristic of a spin-glass-like state.

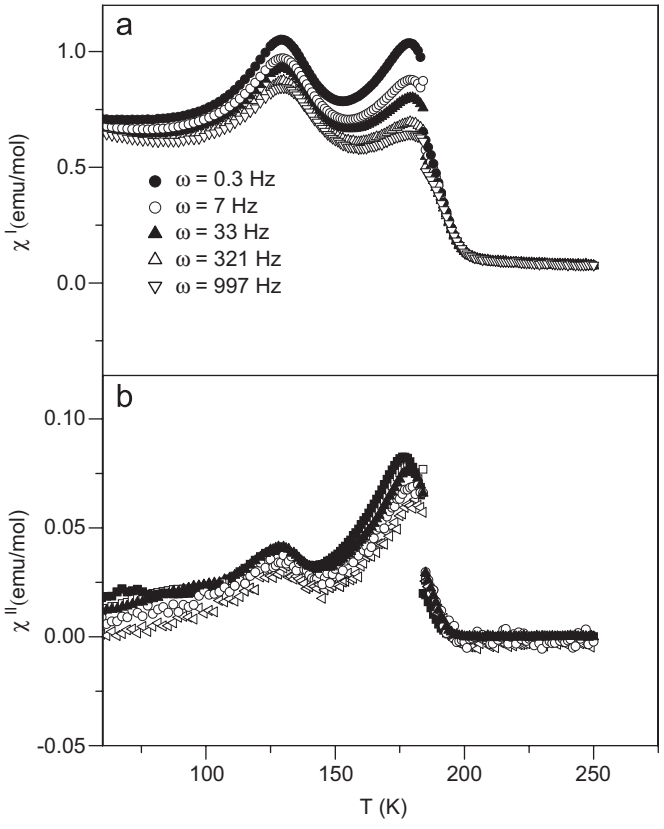


**Fig. 4.** Thermal evolution of the real and imaginary parts of the ac susceptibility.

### 3.2. Crystal structure

The refinement of the crystallographic structure was performed from the NPD patterns acquired at room temperature and at $T = 10$ K in the orthorhombic space group *Pbam*. Firstly, it was assumed that the Mn and Fe atoms occupy, respectively, the 4*f* (0, $\frac{1}{2}$, *z*) and 4*h* (*x*, *y*, $\frac{1}{2}$) sites; however, a better fit was obtained if a certain anti-site disorder was allowed between Mn and Fe atoms. The Fe/Mn occupancy of both sites was refined independently, with no constraints to the chemical formula. The lattice parameters obtained in the refinement and the corresponding discrepancy factors are shown in Table 1. In Table 2, the atomic positions and the occupancy of the Mn/Fe cations are presented. At room temperature, the 4*f* site is occupied at 92.0(8)% by the Mn atoms and 8.0(8)% of Fe atoms; at the 4*h* site the disorder is very similar, since it is occupied at 91.8(10)% and 8.2(10)% by Fe and Mn

**Table 1**
Lattice parameters and reliability factors after the Rietveld refinements from NPD data at 295 K with $\lambda = 1.494$ Å and 10 K with $\lambda = 1.886$ Å

| $T$ (K) | 295 | 10 |
|---|---|---|
| $a$ (Å) | 7.3136(7) | 7.3041(7) |
| $b$ (Å) | 8.5246(8) | 8.5185(7) |
| $c$ (Å) | 5.6927(5) | 5.6887(5) |
| $V$ (Å$^3$) | 354.92(5) | 353.95(5) |
| $R_p$ (%) | 1.55 | 1.98 |
| $R_{wp}$ (%) | 1.98 | 2.52 |
| $R_{exp}$ (%) | 1.20 | 1.28 |
| $\chi^2$ | 2.73 | 3.89 |
| $R_{Bragg}$ (%) | 5.47 | 6.51 |
| $R_{mag}$ (%) | – | 12.6 |

**Table 2**
Atomic parameters after the refinement of the crystallographic structure from NPD data at 295 K with $\lambda = 1.494$ Å and 10 K with $\lambda = 1.886$ Å

| $T$ (K) | | 295 | 10 |
|---|---|---|---|
| Dy | $x$ | 0.1359(8) | 0.1368(6) |
| | $y$ | 0.1691(3) | 0.1698(6) |
| | $B$ (Å$^2$) | 0.72(6) | 0.86(8) |
| Mn/Fe | $z$ | 0.255(3) | 0.254(7) |
| | $B$ (Å$^2$) | −0.02(2) | −0.8(7) |
| | Occup(%) | 0.920(8)/0.080(8) | 0.92(2)/0.08(2) |
| Fe/Mn | $x$ | 0.3849(9) | 0.389(1) |
| | $y$ | 0.3564(6) | 0.3581(8) |
| | $B$ (Å$^2$) | 0.8(1) | −0.6(2) |
| | Occup(%) | 0.918(10)/0.082(10) | 0.82(2)/0.18(2) |
| O1 | $z$ | 0.265(2) | 0.261(3) |
| | $B$ (Å$^2$) | 0.7(1) | 1.1(2) |
| O2 | $x$ | 0.159(1) | 0.152(2) |
| | $y$ | 0.445 (1) | 0.445(1) |
| | $B$ (Å$^2$) | 1.2(1) | 1.4(2) |
| O3 | $x$ | 0.150(1) | 0.148(2) |
| | $y$ | 0.430(1) | 0.428(1) |
| | $B$ (Å$^2$) | 1.0(1) | 1.2(2) |
| O4 | $x$ | 0.3951(8) | 0.396(1) |
| | $y$ | 0.2062(6) | 0.2068(8) |
| | $z$ | 0.2387(8) | 0.238(1) |
| | $B$ (Å$^2$) | 0.44(9) | 0.4(1) |

Sites: Dy and O2 in 4*g* (*x*, *y*, 0), Mn 4*f* (0, $\frac{1}{2}$, *z*), Fe and O3 in 4*h* (*x*, *y*, $\frac{1}{2}$), O1 in 4*e* (0, 0, *z*) and O4 in 8*i* (*x*, *y*, *z*).

atoms, respectively. The most characteristic atomic distances and bonding angles are presented in Table 3. The good agreement between the observed and calculated NPD patterns in the final Rietveld fit can be appreciated in Fig. 5(a). The second series of Bragg reflections correspond to vanadium from the double-walled sample holder; the third row accounts for the Bragg reflections of a $DyMnO_3$ minor impurity, found during the refinement process.

**Table 3**
Selected interatomic distances (Å) and bond angles (deg)

| $T$ (K) | 295 | 10 |
|---|---|---|
| Dy–O1 (*x*2) | 2.312(9) | 2.30(1) |
| Dy–O2 | 2.362(9) | 2.35(1) |
| Dy–O2 | 2.42(1) | 2.46(1) |
| Dy–O4 (*x*2) | 2.354(6) | 2.351(8) |
| Dy–O4 (*x*2) | 2.465(6) | 2.454(8) |
| ⟨Dy–O⟩ | 2.381(8) | 2.378(9) |
| Fe–O1 (*x*2) | 1.999(8) | 1.99(1) |
| Fe–O3 | 1.82(1) | 1.86(1) |
| Fe–O4 (*x*2) | 1.964(6) | 1.971(8) |
| ⟨Fe–O⟩ | 1.949(8) | 1.956(9) |
| Mn–O2 (*x*2) | 1.92(1) | 1.88(3) |
| Mn–O3 (*x*2) | 1.88(1) | 1.87(3) |
| Mn–O4 (*x*2) | 1.920(6) | 1.919(7) |
| ⟨Mn–O⟩ | 1.907(9) | 1.90(2) |
| Mn–Mn | 2.90(2) | 2.90(5) |
| Mn–Mn | 2.79(2) | 2.80(5) |
| Fe–Fe | 2.972(8) | 2.91(1) |
| Fe–O1–Fe | 96.0(5) | 94.0(7) |
| Mn–O2–Mn | 98.3(12) | 100(3) |
| Mn–O3–Mn | 96.0(12) | 97(3) |
| Mn–O3–Fe | 131.2(8) | 130.7(14) |
| Mn–O4–Fe | 125.2(5) | 125.1(9) |

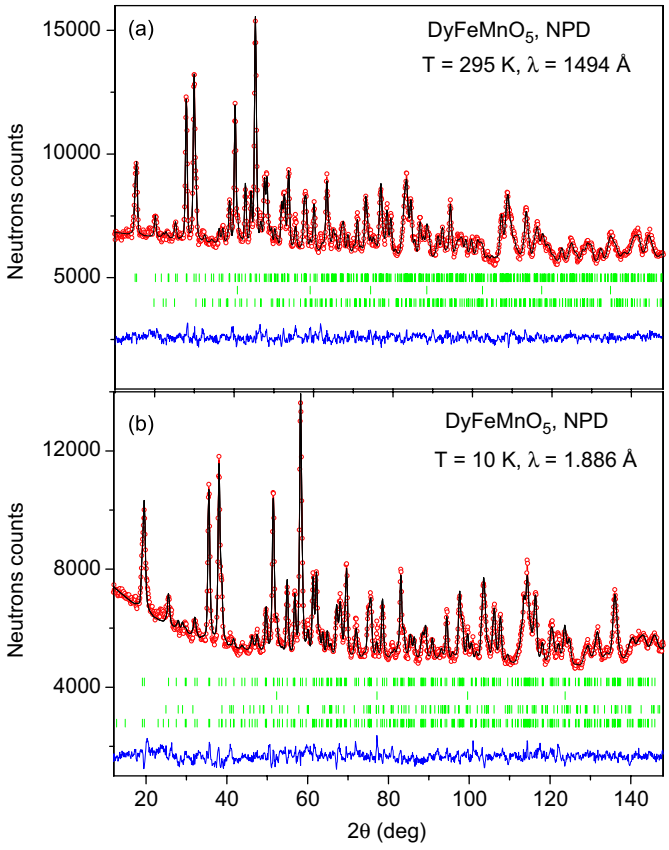


**Fig. 5.** Comparison of the observed (circles), calculated (solid line) and difference (at the bottom) NPD patterns. (a) At room temperature; the three series of tick marks correspond to the positions of the allowed Bragg reflections for the main phase, vanadium and $DyMnO_3$. (b) At $T = 10$ K; the fourth series of tick marks correspond to the magnetic reflections.

The crystallographic structure at $T = 10$ K has also been refined from NPD data with a longer wavelength, 1.886 Å; at this temperature $DyFeMnO_5$ is magnetically ordered; therefore the magnetic contribution to the NPD pattern was taken into consideration. After including the magnetic structure described below, it was observed that the crystallographic structure remains virtually unchanged, also defined in the space group *Pbam*. The lattice parameters and discrepancy factors, atomic positions and the most important atomic distances and bonding angles are also included in Tables 1–3. As it can be observed in Table 2, the anti-site disorder between the Fe and Mn cations is very similar to that found at room temperature. The experimental and calculated NPD patterns are compared in Fig. 5(b).

In Fig. 6, a projection of the crystallographic structure along the *c*-axis is presented. $Mn^{4+}$ cations (mainly occupying the 4*f* site) are at the centre of $Mn^{4+}O_6$ octahedra which share edges via the equatorial O2 and O3 oxygens, forming infinite chains along the *c*-axis. The $Fe^{3+}$ cations (mainly located at the 4*h* site) are coordinated to five closer neighbouring oxygens in a pyramidal configuration; in the $Fe^{3+}O_5$ pyramids the O3 oxygen is in the axial position and the O1 and O4 oxygens are in the equatorial plane. Two $Fe^{3+}O_5$ pyramids, doubly linked by O1 oxygens, form a dimer unit $Fe_2O_{10}$. In this way, four $Mn^{4+}O_6$ octahedra chains are linked by these dimer units through the O3 and O4 oxygens.

### 3.3. Magnetic structure

In the 10 K diagram there is an additional contribution to the scattering on the low-angle Bragg positions, characteristic of a ferri- or ferromagnetic (FM) ordering, since the size of the magnetic unit cell coincides with the chemical one, and therefore the magnetic structure can be defined with a propagation vector $\mathbf{k} = 0$. A good agreement between the calculated and the experimental intensities was obtained in a trial model considering the Mn and Fe spins ordered in an arrangement given by the basis vectors (0, 0, $F_z$) and (0, 0, $F_z'$), respectively. The coupling between

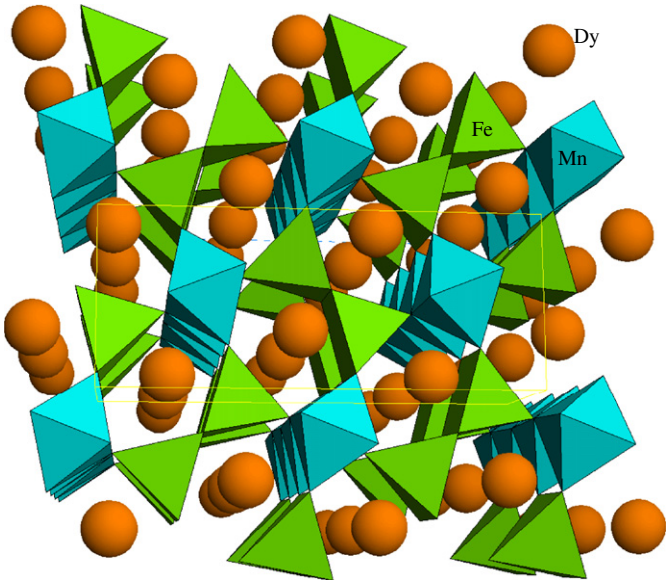


**Fig. 6.** View of the crystallographic structure of $DyFeMnO_5$ along the *c*-axis. Octahedra and tetragonal pyramids correspond to $Mn^{4+}O_6$ and $Fe^{3+}O_5$ polyhedra. The octahedra share edges, forming infinite chains along the *c*-axis. The pyramids form dimer units, linking together the chains of octahedra. The spheres represent the Dy atoms.

the Mn and Fe sublattices is AFM (antiparallel spins), which implies a global ferrimagnetic structure. In a second step the magnetic scattering from the $Dy^{3+}$ cations was also introduced, given by the basis vector (0, 0, $F_z''$), obtaining an additional improvement of the Rietveld fit. Experimentally we found an arrangement corresponding to a parallel alignment of the $Dy^{3+}$ moments with those of the $Fe^{3+}$ sublattice. After the final refinement at 10 K, considering the whole crystal structure and the magnitude of the moments for Fe, Mn and Dy atoms, we found a *z*-component of the magnetic moments of $-1.2(2)\mu_B$ for the $Mn^{4+}$ cations, $2.6(6)\mu_B$ for the $Fe^{3+}$ cations and $2.6(8)\mu_B$ for the $Dy^{3+}$ cations (Table 4). Dy magnetic moments are parallel to those of Fe and antiparallel to the Mn spins, keeping a global ferrimagnetic structure at low temperature. Fig. 7 depicts a schematic view of the magnetic structure. The good agreement between the experimental and calculated NPD patterns is illustrated in Fig. 5(b), where the fourth series of Bragg reflections corresponds to the magnetic model.

## 4. Discussion

$DyFeMnO_5$ derives from the parent $DyMn_2O_5$ oxide (containing one $Mn^{3+}$ and one $Mn^{4+}$ cation per formula) by full replacement of $Mn^{3+}$ by $Fe^{3+}$ cations. The crystal structure of $DyFeMnO_5$ refined by NPD data is closely related to that of $DyMn_2O_5$ [19] oxide, as expected from the similarity in ionic radii between $Fe^{3+}$ and $Mn^{3+}$, of 0.645 Å in six-fold coordination and high-spin state for both cations [20]. In fact, the unit-cell volume for $DyMn_2O_5$, 354.91 $Å^3$ [19], is similar to that of $DyFeMnO_5$, 354.92(5). Some distinctive features have been found in the bonding distances of the $Mn^{4+}O_6$, $Fe^{3+}O_5$ and $Dy^{3+}O_8$ polyhedra. Regarding the $Mn^{4+}O_6$ octahedra the changes are little significant; the average bonding distance value is 1.918(2) Å in $DyMn_2O_5$ and 1.907(9) Å in $DyFeMnO_5$. In both cases the $Mn^{4+}O_6$ octahedra are flattened, since the three Mn–O distances are different; the Mn–O3 and Mn–O2 bonds in the equatorial plane correspond to the shorter and longer distances, respectively. In the tetragonal pyramids, as illustrated in Table 3, the substitution of $Mn^{3+}$ by $Fe^{3+}$ originates a shortening of the axial bonding distance Fe–O3 (1.82(1) Å) and a lengthening of the equatorial bonding distances Fe–O4 (1.964(6) Å) and Fe–O1 (1.999(8) Å), with a slight average expansion of the pyramidal units: the average bonding distance is 1.939(2) Å in $DyMn_2O_5$ and 1.949(8) Å in $DyFeMnO_5$. The changes observed in the tetragonal pyramids cannot be related to the ionic radii, since $Mn^{3+}$ and $Fe^{3+}$ have the same tabulated value; they are very possibly linked to the Jahn–Teller character of the $Mn^{3+}$ cations, which favour the lengthening of the axial bond lengths in the $Mn^{3+}O_5$ pyramids, in contrast with the non-Jahn–Teller configuration of $Fe^{3+}$. It seems that the substitution of $Fe^{3+}$ by $Mn^{3+}$ cations induce the $Fe^{3+}$ cations to shift towards the pyramid apex. Finally, in the $Dy^{3+}O_8$ polyhedron, although some slight variations in the individual Dy–O bonding distances are observed, the average ⟨Dy–O⟩ distances are very similar, 2.389(2) Å in $DyMn_2O_5$ and 2.381(8) Å in $DyFeMnO_5$.

**Table 4**
Results obtained after the refinement of the magnetic structure at $T = 10$ K with a reliability factor $R_{mag} = 12.6\%$

| | $Mn^{4+}$ | $Fe^{3+}$ | $Dy^{3+}$ |
|---|---|---|---|
| Solution | (0, 0, $F_z$) | (0, 0, $F_z'$) | (0, 0, $F_z''$) |
| *z*-Component ($\mu_B$) | −1.2(2) | 2.6 (6) | 2.6 (8) |

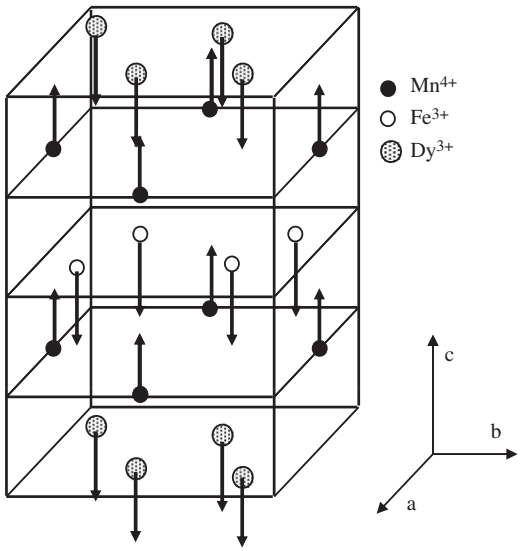


**Fig. 7.** A view of the magnetic structure. There is a FM coupling of $Fe^{3+}$ and $Dy^{3+}$ moments, and AFM with those of $Mn^{4+}$.

Magnetic susceptibility data together with neutron diffraction experiments demonstrate that $DyFeMnO_5$ is a ferrimagnet with a $T_C = 178$ K. Although we only have available NPD data at RT and 10 K, we can speculate that the long-range magnetic order only concerns the $Mn^{4+}$ and $Fe^{3+}$ magnetic moments immediately below $T_C$; the onset of FM ordering is clearly defined in the ac-susceptibility curves (Fig. 4). Located at the *4f* and *4h* crystallographic sites of the *Pbam* space group, respectively, the Mn and Fe moments lie along the *z* direction and are antiferromagnetically coupled, giving rise to a global ferrimagnetic structure. A second anomaly observed in the ac-susceptibility at 130 K (Fig. 4) coincides with the splitting of ZFC and FC dc-susceptibility curves; we suggest the establishment of a partial freezing of the magnetic moments, since the maximum of the ac-susceptibility curves is frequency dependent. At a lower temperature, at around 20 K, as indicated by the sudden rise of the FC curve, the $Dy^{3+}$ sublattice participates in the magnetic structure, induced by a polarization from the $Fe^{3+}$ sublattice; the low-temperature magnetic structure studied at 10 K by NPD indicates a FM coupling of the $Dy^{3+}$ and $Fe^{3+}$ moments directed along **c**; the coupling between the $Dy^{3+}$ and the $Mn^{4+}$ sublattices is, therefore, AFM. It is worth commenting that the magnetization isotherm at $T = 1.8$ K (Fig. 3) shows a maximum magnetization close to $7\mu_B$/f.u., which is much larger than the $2\mu_B$/f.u. expected for a perfect ferrimagnetic coupling of high-spin $Fe^{3+}$ ($3d^5$, $S = \frac{5}{2}$) and $Mn^{4+}$ ($3d^3$, $S = \frac{3}{2}$) spins, obviously containing an important contribution from the $Dy^{3+}$ magnetic moments, ferromagnetically aligned to the $Fe^{3+}$ spins, as shown from NPD data, and strongly polarized by the external magnetic field.

It is remarkable that the ordered magnetic moments refined from NPD data at 10 K for Mn, Fe and Dy, of 1.2, 2.6 and $2.6\mu_B$, respectively, are very much reduced with respect to those expected for $Mn^{4+}$ ($3d^3$, $3\mu_B$ ), $Fe^{3+}$ ($3d^5$, $5\mu_B$) and $Dy^{3+}$ ($^6H_{15/2}$, $\approx 10\mu_B$). The lack of a full long-range ordering can be related with the observed divergence of FC and ZFC susceptibility curves and the presence of a frequency dependence peak in the ac-susceptibility curves at 130 K, defining the onset of a frustrated, spin-glass-like system. Perhaps this partial magnetic disordering can be related with the observed antisite between Fe and Mn positions. It is well known that the $Mn^{4+}$–O–$Mn^{4+}$ superexchange interactions are FM in origin when the angles are close to 90°, as defined by the Goodenough–Kanamori rules [21,22]; in an ideal scenario this fact would account for the FM coupling of $Mn^{4+}$ spins along the chains of octahedra. Let us remember that $MnO_6$

octahedra share edges along the *c* direction, with Mn–O2–Mn and Mn–O3–Mn angles in the 96–98° range (Table 3). The same FM coupling is expected within the pairs of $Fe^{3+}$–O–$Fe^{3+}$ conforming each dimmer unit, with superexchange angles close to 90° boosting the FM interactions in the Fe sublattice. However, the antisite of some $Fe^{3+}$ into the chains of $MnO_6$ octahedra and $Mn^{3+}$ into the dimer $Fe_2O_{10}$ units would promote strong antiferromagnetic interactions in both structural motifs, as predicted by Goodenough [21]. The competing presence of predominant FM together with AFM interactions in each sublattice can be the driving force for the magnetic disorder and frustration detected by the macroscopic measurements, and the relatively weak magnetic moments refined on the Fe, Mn and Dy sites.

Finally, it is worth proposing the possibility that $Fe^{3+}$ spins within the dimmer units are already coupled (but not long-range ordered) above $T_C$. As displayed in the inset of Fig. 2, there is an abrupt change in the reciprocal dc susceptibility at 220 K that could be coinciding with the onset of such short-range interactions. The paramagnetic state is only reached above this temperature. It is noteworthy that the paramagnetic temperature estimated from the Curie–Weiss fit above 220 K is very small ($\theta_P = 9.29(8)$ K), which can reflect a balance between the strongly positive interactions between $Fe^{3+}$ within the dimer units and the Fe–O–Mn antiferromagnetic interactions between both magnetic sublattices, characteristic of every ferrimagnetic system, which below $T_C$ will give rise to the establishment of a three-dimensional ferrimagnetic structure.

## 5. Conclusions

A new ferrimagnetic compound, $DyFeMnO_5$, with $T_C = 178$ K, has been prepared by a wet-chemistry synthesis procedure followed by a thermal treatment under high oxygen pressure conditions. The crystallographic structure, studied from NPD data, is similar to that of the parent $DyMn_2O_5$ oxide, defined in the orthorhombic *Pbam* space group, and it consists of infinite chains of edge-sharing $Mn^{4+}O_6$ octahedra arranged along the *c*-axis; the chains are linked by pairs of $Fe^{3+}O_5$ corner-sharing pyramids, with the $Dy^{3+}$ cations arranged in voids with eight-fold oxygen coordination. A certain cationic disorder (about 8%) has been found over the 4*f* and 4*h* sites, ideally occupied by the $Mn^{4+}$ and $Fe^{3+}$ cations, respectively. In contrast with $DyMn_2O_5$, showing elongated $Mn^{3+}O_5$ pyramids, the $Fe^{3+}O_5$ units in $DyFeMnO_5$ are flattened; this difference is ascribed to the Jahn–Teller character of the $Mn^{3+}$ cations.

Magnetization and NPD data show that $DyFeMnO_5$ is a ferrimagnet with $T_C \approx 178$ K; the magnetic structure is characterized by $\mathbf{k} = 0$, consisting of an antiferromagnetic arrangement of $Fe^{3+}$ and $Mn^{4+}$ spins, aligned along the *c*-axis. $Dy^{3+}$ moments become polarized below 20 K, ferromagnetically coupled to the $Fe^{3+}$ sublattice and antiferromagnetically coupled to the $Mn^{4+}$ sublattice. At $T = 10$ K the refined magnetic moments values are $-1.2(2)\mu_B$ for the $Mn^{4+}$ cations, $2.6(6)\mu_B$ for the $Fe^{3+}$ cations and $2.6(8)\mu_B$ for the $Dy^{3+}$ cations. Their strong reduction with respect to the expected values is related to the antisite disordering in both sublattices, promoting AFM interactions that partially hinder the FM coupling in the chains of $MnO_6$ octahedra and in the $Fe_2O_{10}$ dimmers, leading to a certain degree of magnetic frustration detected by the macroscopic measurements and accounting for the relatively weak magnetic moments refined on the Fe, Mn and Dy sites.

## Acknowledgments

We thank the financial support of the Spanish Ministry of Education to the project MAT2007-60536. This work was partially performed at the spallation source SINQ, Paul Scherrer Institute, Villigen, Switzerland.

## References

[1] W. Eerenstein, N.D. Mathur, J.F. Scott, Nature 442 (2006) 759.
[2] H. Schmid, Ferroelectrics 162 (1994) 317.
[3] R.E. Cohen, J. Phys. Chem. Solids 61 (2000) 139.
[4] T. Kimura, T. Goto, H. Shintani, K. Ishizaka, T. Arima, Y. Tokura, Nature (London) 426 (2003) 55.
[5] T. Goto, T. Kimura, G. Lawes, A.P. Ramirez, Y. Tokura, Phys. Rev. Lett. 92 (2004) 257201.
[6] N. Hur, S. Park, P.A. Sharma, J.S. Ahn, S. Guha, S.-W. Cheong, Nature (London) 429 (2004) 392.
[7] N. Hur, S. Park, P.A. Sharma, S. Guha, S.-W. Cheong., Phys. Rev. Lett. 93 (2004) 107207.
[8] G.R. Blake, L.C. Chapon, P.G. Radaelli, S. Park, N. Hur, S.-W. Cheong, J. Rodríguez-Carvajal, Phys. Rev. B 71 (2005) 214402.
[9] E.F. Bertaut, G. Buisson, A. Durif, A. Mareschal, M.C. Montmorry, Quezel-Ambrunaz, Bull. Soc. Chim. Fr. (1965) 1132.
[10] J.A. Alonso, M.T. Casais, M.J. Martínez-Lope, I. Rasines, J. Solid State Chem. 129 (1997) 105.
[11] J.A. Alonso, M.T. Casais, M.J. Martínez-Lope, J.L. Martínez, M.T. Fernández-Díaz, J. Phys.: Condens. Matter 9 (1997) 8151.
[12] G. Buisson, Phys. Stat. Sol. A 16 (1973) 533.
[13] G. Buisson, Phys. Stat. Sol. A 17 (1973) 191.
[14] A. Muñoz, J.A. Alonso, M.J. Martínez-Lope, J.L. Martínez, Chem. Mater. 16 (2004) 4087.
[15] A. Muñoz, J.A. Alonso, M.J. Martínez-Lope, J.L. Martínez, Eur. J. Inorg. Chem. (2007) 1972.
[16] A. Muñoz, J.A. Alonso, M.J. Martínez-Lope, J.L. Martínez, Phys. Rev. B 72 (2005) 184402.
[17] H.M. Rietveld, J. Appl. Crystallogr. 2 (1969) 65.
[18] J. Rodríguez-Carvajal, Physica B 192 (1993) 55.
[19] S.C. Abrahams, J.L. Bernstein, J. Chem. Phys. 46 (1967) 3376.
[20] R.D. Shanon, Acta Crystallogr. Sect. A 32 (1976) 751.
[21] J.B. Goodenough, Phys. Rev. 100 (1955) 564.
[22] J. Kanamori, J. Phys. Chem. Solids 10 (1959) 87.